Biophysical Journal
Article

Biophysical Society

Collective heterogeneity of mitochondrial potential in contact inhibition of proliferation

Basil Thurakkal,[1] Kishore Hari,[2] Rituraj Marwaha,[1] Sanjay Karki,[1] Mohit K. Jolly,[2,*] and Tamal Das[1,*]
[1]Tata Institute of Fundamental Research Hyderabad (TIFR-H), Hyderabad, India and [2]Centre for BioSystems Science and Engineering, Indian Institute of Science, Bengaluru, India

ABSTRACT In the epithelium, cell density and cell proliferation are closely connected to each other through contact inhibition of proliferation (CIP). Depending on cell density, CIP proceeds through three distinct stages: the free-growing stage at low density, the pre-epithelial transition stage at medium density, and the post-epithelial transition stage at high density. Previous studies have elucidated how cell morphology, motion, and mechanics vary in these stages. However, it remains unknown whether cellular metabolism also has a density-dependent behavior. By measuring the mitochondrial membrane potential at different cell densities, here we reveal a heterogeneous landscape of metabolism in the epithelium, which appears qualitatively distinct in three stages of CIP and did not follow the trend of other CIP-associated parameters, which increases or decreases monotonically with increasing cell density. Importantly, epithelial cells established a collective metabolic heterogeneity exclusively in the pre-epithelial transition stage, where the multicellular clusters of high- and low-potential cells emerged. However, in the post-epithelial transition stage, the metabolic potential field became relatively homogeneous. Next, to study the underlying dynamics, we constructed a system biology model, which predicted the role of cell proliferation in metabolic potential toward establishing collective heterogeneity. Further experiments indeed revealed that the metabolic pattern spatially correlated with the proliferation capacity of cells, as measured by the nuclear localization of a pro-proliferation protein, YAP. Finally, experiments perturbing the actomyosin contractility revealed that, while metabolic heterogeneity was maintained in the absence of actomyosin contractility, its *ab initio* emergence depended on the latter. Taken together, our results revealed a density-dependent collective heterogeneity in the metabolic field of a pre-epithelial transition-stage epithelial monolayer, which may have significant implications for epithelial form and function.

SIGNIFICANCE Epithelial contact inhibition of proliferation (CIP) plays a key role in tissue homeostasis, morphogenesis, and development. The biochemical changes in cells during different stages of CIP are not as well documented as the biophysical changes. We unveil a heterogeneous landscape of metabolism that appears distinct in different stages of CIP. Importantly, in the pre-epithelial transition stage, epithelial cells establish a collective metabolic heterogeneity where multicellular clusters of high- and low-potential cells emerge despite the uniform genetic and nutrient conditions for the cells. The collective heterogeneity is correlated with local fluctuations in geometrical parameters and the proliferative capacity of cells. Finally, we demonstrate the role of cell mechanics in establishment of collective heterogeneity.

INTRODUCTION

Orchestration of cell proliferation and growth in the epithelial tissue is pivotal for morphogenesis, tissue homeostasis, and development in multicellular organisms (1). This feat is achieved by strict control over processes like cell division, apoptosis, cell migration, and metabolism. An important way of regulating cell proliferation in the epithelium is contact inhibition of proliferation (CIP). CIP is defined as a decrease in the mitotic rate of cells when a critical density is attained (2,3). When reaching this critical density, cell-cell junctions and the intracellular molecular signaling undergo significant changes that prevent the cells to enter the cell division cycle. Importantly, CIP also marks the transition from the free-growing motile state to the highly dense immobile state of epithelial cells (4). Loss of CIP can result in cancer and abnormal morphogenesis (5). Relevantly, depending on mitotic rate patterns, cell shape, and cell density, CIP proceeds through three distinct stages (4). At

Submitted January 10, 2023, and accepted for publication August 17, 2023.

*Correspondence: mkjolly@iisc.ac.in or tdas@tifrh.res.in

Sanjay Karki's present address is Aix Marseille Université, CNRS, IBDM-UMR7288, Turing Center for Living Systems, 13007 Marseille, France.

Editor: Padmini Rangamani.

https://doi.org/10.1016/j.bpj.2023.08.014

low density, cells continue to divide without any decrease in cell mitotic rate. Epithelial cells are observed to have a stretched, spindle-shaped morphology at low density. At medium density, the cells undergo a morphological transition, acquiring a polygonal epithelial shape. Finally, at the highest density, mitotic arrest happens, and the cell area continues to decrease and induce kinetic arrest (4,6). Hereafter, we refer to these three distinct stages as stages 1, 2, and 3, respectively. Relevantly, while some of the biophysical features of these stages of CIP are known, they remain mostly uncharacterized from a biochemical point of view.

Nevertheless, CIP is known to be the cause and result of mechanical and biochemical changes in the epithelial cells (7–10). As the density increases, stronger cadherin-mediated cell-cell contacts are made, resulting in mechanical changes such as decreasing traction forces (7–9). These changes eventually act as inhibitory signals, resulting in a mitotic arrest (4,11–14). The increase in density and contact inhibition is also accompanied by a glass-like phase transition in epithelial cells (15). At a cell-autonomous level, the mechanism behind the mechanical signaling of CIP is linked to the Hippo signaling pathway. It is known that cell size and shape deformations trigger the Hippo pathway to cause CIP (6,14,16–18). On the other hand, the epithelial growth factor level is one of the main biochemical cues known for regulating CIP because cadherin-mediated contacts inhibit cell proliferation only when epithelial growth factor is below a critical threshold level (10). Taken together, most of the studies so far focus on the mechanisms of CIP or biophysical changes associated with CIP. However, the metabolic changes the cell undergoes while approaching CIP remain elusive.

Metabolic changes are an important aspect associated with cell growth and proliferation (19). Rapidly proliferating cancer cells that multiply quickly tend to favor aerobic glycolysis as their primary metabolic pathway instead of the more efficient oxidative phosphorylation (20,21). Known as the Warburg effect, it is a characteristic of not only cancer cells but also normal proliferating cells (22). It is well established that the mitochondrion, being the powerhouse of a cell, has an immense role in cellular metabolism as a biosynthesis center, balancer of reducing equivalents, and waste management hub (23). It is possible that malignant cells prefer the glycolytic pathway because of inherent mitochondrial deficiencies. In addition, mitochondrial outer membrane permeabilization plays a crucial role in regulated cell death (24–26), and many cancer cells exhibit increased resistance to regulated cell death because of alterations in mitochondrial control of the process (5). Hence it is important to look at the changes in metabolism, and specifically mitochondrial activity changes, in the context of control of proliferation and CIP. Previous studies have explored the global metabolic changes of cells as cell density increases. The population-averaged studies, focusing on metabolic changes with increasing density, have revealed that metabolic pointers like oxygen consumption level, net lactate production, ATP content, and total nicotinamide adenine dinucleotide content per cell decrease with increasing cell density (27). However, the spatiotemporal changes in cell metabolism as CIP progresses through the three stages remain unknown. Here we investigated the cellular- and multicellular-scale dynamics of metabolism accompanied by different stages of CIP. We asked how metabolism might be correlated with the geometrical and mechanical parameters of epithelial cells in the three stages of CIP.

MATERIALS AND METHODS

Cell culture

Madin-Darby canine kidney (MDCK) epithelial cell lines were used for this study. Tetracycline-resistant wild-type MDCK cell lines were a gift from Yasuyuki Fujita. Cells were cultured in Dulbecco's modified Eagle's medium (DMEM) supplemented with GlutaMax (Gibco) with 5% fetal bovine serum (tetracycline-free fetal bovine serum [FBS], Takara Bio) and 10 U mL^{-1} penicillin and 10 μg mL^{-1} streptomycin (Invitrogen) in an incubator maintained at 37°C and 5% CO_2 unless mentioned otherwise. All transient plasmid DNA transfections were done using Lipofectamine 2000 (Invitrogen) following the manufacturer's protocol. We varied the density of cultured cells by increasing the seeding density. To get a higher density with the desired control, the cells were seeded in an Ibidi two-well insert.

Staining for the mitochondrial membrane potential ($\Delta\Psi_M$)

We used either 2 μg/mL 5,5,6,6′-tetrachloro-1,1′,3,3′ tetraethylbenzimi-dazoylcarbocyanine iodide (JC-1) dye (Invitrogen) or 100 nM tetramethylrhodamine methyl ester perchlorate (TMRM; catalog number I34361, Invitrogen) to stain for $\Delta\Psi_M$. The cells were incubated at 37°C for 30 min with TMRM to stain the cells. Following incubation, cells were imaged immediately in TMRM-containing medium. In the case of JC-1 imaging, the dye-containing medium was replaced with DMEM prior to imaging.

Antibodies and plasmids

Sources and dilutions of all primary and secondary antibodies used for the immunostaining studies are given in Table S1. The details of all plasmids used for this study are given in Table S2.

Immunofluorescence

Cell fixation was done with 4% formaldehyde diluted in 1× phosphate-buffered saline (PBS; pH 7.4) at room temperature (RT) for 10 min, followed by 1× PBS washes (three times). Cell permeabilization was carried out with 0.25% (v/v) Triton X-100 (Sigma) in PBS for 10 min at RT, followed by washing three times with PBS to remove the reagent. To block non-specific antibody binding, samples were incubated in 2% BSA in 0.1% (v/v) PBST (Triton X-100 in 1× PBS) at RT for 45 min. The blocking buffer was removed after 45 min, and the primary antibody dilution prepared in the blocking buffer was added to the samples for 60 min at RT or at 4°C overnight. Afterward, samples were washed twice with PBST and three times with 1× PBS. Next, secondary antibodies tagged with a fluorophore were (same dilution as primary) prepared in blocking buffer and added to the sample for 60 min at RT. To counterstain cell nuclei, the

samples were added with a DNA-binding dye, 4′,6-diamidino-2-phenylindole (DAPI; 1 μg mL^{-1} in PBS, Invitrogen), along with the secondary antibody solution. Last, thorough washing of the samples was done with PBST and PBS before imaging.

5-Ethynyl-2′-deoxyuridine (EdU) proliferation assay

We used the Click-iT Plus EdU Cell Proliferation Kit (Invitrogen, C10637) and Click-iT EdU Imaging Kit (Invitrogen, C10086) for the proliferation assay. MDCK cells were seeded to confluence at the required density in a glass-bottom dish. The cells were incubated at 37°C in 10 μM EdU diluted in complete DMEM for 60 min, followed by cell fixation with 4% formaldehyde diluted in 1× PBS (pH 7.4) at RT for 15 min. The fixation medium was removed, and the cells were washed twice with 3% BSA solution in PBS. After washing, cell permeabilization was carried out with 0.5% (v/v) PBST at RT for 20 min. Click chemistry reactions were carried out following the manufacture's standard protocol for each kit. Last, the samples were counterstained for cell nuclei using DAPI (1 μg mL^{-1} in PBS, Invitrogen) before imaging using wide-field microscopy.

Wide-field microscopy

Wide-field fluorescence images were acquired using a 20× air objective (HC PL FLUOTAR L PH1 20×, numerical aperture = 0.4, Leica) mounted on a Leica DMi8 microscope. Images were acquired using a Leica DFC9000 scientific CMOS camera. Time-lapse images were taken in a stage-top live chamber maintained at 37°C and 5% CO_2.

Confocal microscopy

Fluorescence images were acquired using a 60× oil objective (PlanApo N 60× Oil, numerical aperture = 1.42, Olympus) mounted on an Olympus IX83 inverted microscope equipped with a scanning laser confocal head (Olympus FV3000). Time-lapse images of live samples were done in the live-cell chamber provided with the microscopy setup. 25 mM 4-(2-hydroxyethyl)-1-piperazineethanesulfonic acid buffer (Gibco) was used to maintain pH levels.

Inhibition studies

For all inhibition studies, cells in glass-bottom dishes were incubated with the required concentration of the inhibitor in OptiMEM and TMRM (mitochondrial potential dye) for 30 min at 37°C in a 5% CO_2 humidified incubator for pre-treatment. Cells were switched to TMRM-containing growth medium (Fluorobrite DMEM + 5% FBS) with or without inhibitors according to the experimental setup and imaged on a wide-field fluorescence microscope. The cells were treated with 5 μM carbonyl cyanide 4-(trifluoromethoxy)phenylhydrazone (FCCP; Sigma, a mitochondrial potential decoupler) for 1 h to short-circuit the potential across the mitochondrial membrane. For recovery post FCCP treatment, the cells were replenished with growth medium containing the myosin II inhibitor blebbistatin (Sigma, B0560, 50 μM) and Rho-associated protein kinase (ROCK) inhibitor Y27632 (Sigma, 30 μM), to disrupt the actomyosin contractility. All drugs were dissolved in DMSO to prepare the primary stock solution.

Cells cycle stage synchronization using aphidicolin

MDCK cells were grown in complete DMEM with 5% FBS to 70% confluency before switching to complete medium with 10 μg mL^{-1} aphidicolin concentration. Cells were then grown to confluency overnight (30 h) in the presence of aphidicolin. After 30 h, aphidicolin treatment was released by replacing the medium with complete medium with 5% FBS. Images were taken 1.5 h post release.

Fluorescence resonance energy transfer (FRET)-based molecular tension and metabolite measurements

Pyruvate, glucose, and lactate levels in the cells were measured by the FRET-based sensors Pyronic/pcDNA3.1(-), Laconic/pcDNA3.1(-), and pcDNA3.1 FLII12Pglu-700uDelta6, respectively. The FRET experiments were carried out in the live-cell confocal setup (Olympus FV3000). MDCK cells, plated in a six-well plate (Tarsons), were transiently transfected with the corresponding plasmid. After 6 h, cells were trypsinized and seeded in glass-bottom dishes. After confluency, the medium was replaced with fresh medium containing TMRM and 25 mM 4-(2-hydroxyethyl)-1-piperazineethanesulfonic acid. The cells were incubated at 37°C for 30 min before imaging. Images were taken in three different channels: 1) mTFP1 (445 nm laser; filter, 460–500 nm), 2) FRET (445 nm laser; filter, 530–630 nm), and 3) mVenus (514 nm laser; filter, 530–630 nm). The pinhole diameter, laser intensity, and exposure times for donor, acceptor, and FRET channels were always kept constant for all experiments. In the same field of views, TMRM intensity was also measured along with these, with an excitation wavelength of 561 nm. Each field yielded three 1024 × 1024 pixel images representing the donor, FRET, and acceptor channels. Images were then analyzed using custom software written in MATLAB (MathWorks).

Nutrient starvation experiments

For all the nutrient starvation studies, MDCK cells were cultured in complete DMEM to confluency before staining with TMRM and imaged under a fluorescence microscope. Complete DMEM was then replaced with the specified minimal medium containing TMRM. A fluorescence image was then taken after the corresponding incubation time. Details regarding the composition of minimal medium are provided in Table S3.

System biology modeling and simulation

The model can be described as follows.

- A 2D grid (100 × 100 pixels) was used to represent the *in vitro* culture. Each pixel can have a maximum of one cell.
- 500 cells were randomly placed across the whole grid at the start of the simulation.
- Each cell had two key properties: activation level (mitochondrial activity) and proliferation/division time. The division time represented the time taken for a cell to divide and was controlled by CIP, as described below.
- A density was assigned to each cell, calculated as the fraction of cells present in a 5 × 5 square grid around the cell. In other words, each cell was sensitive to 2 grids around it, represented as the R neighborhood, where $R = 2$. At the boundary of the grid, cells could sense only a part of the square to determine the density. The density of a corner cell was calculated as the fraction of pixels that were occupied in a quarter of the square (9 pixels instead of the 25 pixels in the full square). Similarly, the cells on the boundaries sensed 13 pixels. The density is the key aspect of the model because it incorporates the effects of CIP. While it does not measure any mechanical properties of the cells directly, it can be taken as a proxy of the intracellular pressure because the intracellular pressure is only being affected by the density in the *in vitro* culture.
- Both the properties were assumed to depend sigmoidally on the density of the cell as follows:

TABLE 1 Default parameter values for the model

Parameter	Terminology used in figures	Value
R (radius for calculating local density)	R	2
actThresh (activation threshold density)	activation threshold	0.9
divThresh (division threshold density)	division threshold	0.1
nAct (exponent for activation level dependence on density)	activation Hill	5
nDiv (exponent for division time dependence on density)	division Hill	1
divTime (basal division time of the cells)	division time	1.5
divFC (maximum fold change in division time with density)	division time FC	8

$$activation\ level\ =\ \frac{density^{nAct}}{\left(density^{nAct}+actThresh^{nAct}\right)} \quad (1)$$

$$division\ time\ =\ divTime+divTime*(divFC\ -\ 1)*\left(\frac{density^{nDiv}}{density^{nDiv}+divThresh^{nDiv}}\right) \quad (2)$$

As the local density increases, the cells become more active and less likely to divide (CIP). *divTime* represents the basal division rate of the cells and was taken to be 1.5 days, which was closer to the proliferation time of MDCK cells. The *divFC* parameter defined the extent to which cell division slowed down in the culture at high density compared with low density. The exponents *nDiv* and *nAct* represented the sensitivity of the activation level and division time to the density. As shown in the results section, the ultra-sensitivity activation level to density, given by a high value of *nAct*, was necessary for collective heterogeneity.

- Each cell was assigned a lifetime, which was the difference between the current simulation time and the birth time of the cell. When the lifetime crossed the division time of the cell, the cell could divide when there was an empty grid in its *R* neighborhood.
- At each time step, all cells were updated in three ways: their activation level changed based on the local density, their division time was updated based on the local density, and they divided when the cells had space around them and when the lifetime was long enough. The default parameters used for the simulations were as follows.

divTime was taken as 1 (28), thereby setting the time unit of the model as a day, and divFC was inspired from the experimental data (Fig. S1 *a*). Sensitivity analysis was performed for all parameters to establish the effect of different model parameters on the emergence of collective heterogeneity. For each sensitivity analysis, the parameter values were the default ones mentioned in the Table 1, except for the parameter that was the subject of the analysis. For specific parameters, like activation and division thresholds, non-default parameters used were mentioned as the title of the corresponding plot. Figures included in the paper are intended to demonstrate the effect of the parameter on activation dynamics and, thereby, the emergence of collective heterogeneity. Complete data corresponding to the sensitivity analysis of all parameters and the corresponding figure have been included in the GitHub repository. The simulations are carried out using the package *Agents.jl* (29) in *Julia* 1.6.2 The simulation codes are available at https://github.com/askhari139/CollectiveHeterogeeneity.

Heterogeneity index and collectivity index calculation

Heterogeneity index, ħ was calculated as

$$\hbar\ =\ \left(\overline{I_{75\%}}\ -\ \overline{I_{25\%}}\right)/\bar{I} \quad (3)$$

where $\overline{I_{75\%}}$ and $\overline{I_{25\%}}$ are the mean fluorescence intensities of cells with top 25% and bottom 25% fluorescence intensity, respectively. $\bar{I}$ represented the mean fluorescence intensity of the entire population. For extracting spatial information, we first divided the image into regions of interest (ROIs) of varying sizes, and mean ħ was calculated for each ROI size (Fig. S1 *c*).

Image analysis

All image analyses mentioned were done by Fiji, custom-written MATLAB scripts, Tissue Analyzer (30), and Cellpose (31). A custom-written MATLAB script was used for the TMRM intensity collectivity-related analysis in Fig. 1. Also, the analysis of geometric parameters including the local density, area, cell shape index, and aspect ratio, was carried out using custom-written MATLAB scripts. All cell-boundary segmentation was carried out using custom-written MATLAB code or Cellpose. In Fig. 1 *a*, second row, the threshold for determining "high" and "low" fluorescence intensity was set at 25% of the cell with the maximum TMRM fluorescence intensity. Cells with intensities higher than the threshold were classified as "high," while the remaining cells were considered "low." For other figures and analyses involving stage 2 of CIP, two thresholds were utilized. The 75th percentile of the population's intensities marks the "high" threshold, and the 25th percentile marks the "low" threshold. Consequently, this defined the upper quartile ("top 25%") and lower quartile ("bottom 25%") populations.

A custom written MATLAB code was used to calculate the YAP nuclear/cytoplasmic ratio. The YAP ratio is defined as

$$log(I_{Nuc}\ /\ I_{P.Nuc}) \quad (4)$$

where I_{Nuc} is the average YAP intensity in the cell nucleus, and $I_{P.Nuc}$ is the average YAP intensity in the perinuclear region (32). The nucleus for each was segmented from the DAPI-stained fluorescence image using Cellpose. The perinuclear region is the dilated region of the nuclear mask by a structural element of size 2. The cell boundaries were calculated by Voronoi tessellation of the cell centroids.

Bayesian force inference

Relative pressure within each cell was computed using the Bayesian force inference method (33,34). To this end, bright-field phase contrast or differential interference contrast (DIC) images showing the cell boundary in the confluent cell monolayer were segmented using Cellpose (31). The segmentation output was then processed by Tissue Analyzer (30) to assign cell vertices and edges. The output data containing this information were fed into a custom-written

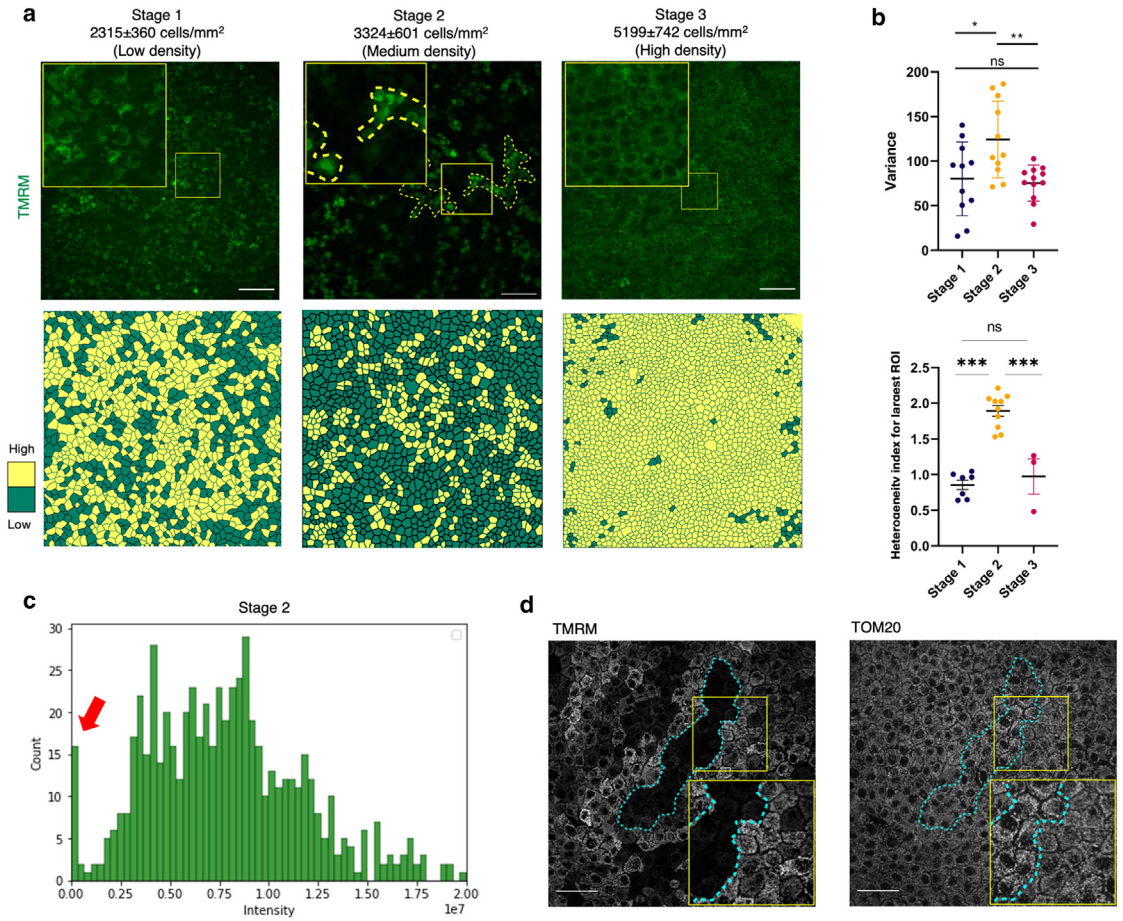

FIGURE 1 Metabolism shows different patterns of collectivity at different stages of CIP. (*a*) *Top*: TMRM-stained images of a confluent MDCK monolayer corresponding to the three stages of CIP, showing differences in the metabolic heterogeneity pattern. Left to right: stages 1, 2, and 3. Yellow dashed lines mark the clusters formed at stage 2. Scale bar, 100 μm. The mean and standard deviation of the cell density corresponding to each stage are shown at the top of the panels. *Bottom*: Cartoon of pattern variation at different global densities corresponding to the field of view. Yellow indicates high $\Delta\Psi_M$ cells, and green squares show low $\Delta\Psi_M$. 25% of the maximum normalized intensity is considered the threshold for low and high classification here. (*b*) *Top*: column scatter-dotplot of variance of TMRM intensity at three stages of CIP in an MDCK cell monolayer. Mean with standard deviation is shown. Statistical significance was assessed using an unpaired Student's *t*-test with Welch's correction (two tailed). *Bottom*: column scatter-dotplot of the heterogeneity index for ROI size equals the image field of view size at three stages of CIP. Mean value is shown along with SEM. Statistical significance was assessed using an unpaired Student's *t*-test. (*c*) Representative histogram showing the distribution of TMRM intensity for cells in stage 2 of CIP. The peak with near-zero intensities is marked by the red arrow. (*d*) Confocal images of TMRM-stained MDCK cells in the *left panel* and *right panel* show Tom20 immunofluorescence confocal images. Scale bar, 50 μm. *p < 0.05, **p < 0.01, and ***p < 0.001. To see this figure in color, go online.

MATLAB (MathWorks) program that implemented Bayesian force inference. As part of this approach, a matrix was formulated to represent the balance between interfacial tensions and intracellular pressure at every vertex of the cell. To solve this undetermined linear system, Bayesian inversion was implemented to calculate all variables and parameters of the problem with a specific probability. Details of the probabilistic determination have been described in detail elsewhere (33). Relative pressure obtained by Bayesian force inference is a unitless quantity.

Normalized relative pressure P_{Norm} is given by

$$P_{Norm} = (P_i - P_{min}) / (P_{max} - P_{min}) \quad (5)$$

where P_i is the calculated relative pressure of the specific cell. $P_{max} = 3 * \text{standard deviation (P)}$ and $P_{min} = -P_{max}$.

The MATLAB program used for the analysis is available in the following GitHub link: https://github.com/askhari139/CollectiveHeterogeeneity.

Statistical analysis

Statistical analyses were carried out in GraphPad Prism 9. Statistical significance was calculated by paired *t*-test with Welch's correction, unpaired Student's *t*-test, or Wilcoxon matched-pairs signed-rank test, as mentioned in the corresponding figure. Bar-whisker plots are displayed as mean ± maximum and minimum values. p values greater than 0.05 were considered to be statistically not significant. For all main and supplementary figures, *p < 0.05, **p < 0.01, and ***p < 0.001. No statistical methods were used to set the sample size. Quantification was done using data from at least three independent biological replicates. For analysis involving live-imaging

experiments, data were collected from at least three independent experiments. All the experiments with representative images were repeated at least three times.

RESULTS

Metabolism shows different collectivity at different stages of CIP

To study the spatiotemporal variation of metabolism associated with CIP, we grew confluent MDCK cell monolayers in varying densities falling into one of three stages. We selected these density values according to the values reported in previous studies (4,15) (Fig. 1 *a*). A cell density range of 2000–2600 cells/mm^2 represented stage 1, which corresponded to the free-growing stage of CIP. Cells at this stage were elongated, with many cells showing stretched triangular or quadrilateral shapes (Fig. 1 *a*), and a significant fraction turned out to be in S phase, as stained by EdU (Fig. S1 *a*). Next, a density range of 2700–4000 cells/mm^2 represents stage 2, which corresponded to the pre-epithelial transition stage of CIP. Cells at this stage showed cobblestone-like hexagonal or higher-order polygonal shapes, but still, a significant fraction turned out to be EdU positive (Figs. 1 *a* and S1 *a*). Finally, in a density range of 4400–6000 cells/mm^2, the fraction of EdU-positive cells decreased with increasing density (Fig. S1 *a*). This density range represented the post-epithelial transition stage of CIP. Importantly, to obtain monolayers with varying densities and, at the same time, to ensure similar culture conditions, we seeded the cells in different initial densities and always imaged them within 24–30 h post seeding. As an indicator of metabolism, especially for oxidative phosphorylation leading to ATP production, we measured $\Delta\Psi_M$ using TMRM, a cell-permeant fluorescent dye. Because the accumulation of TMRM in the mitochondrial matrix is directly proportional to $\Delta\Psi_M$ (35), we can indirectly read out $\Delta\Psi_M$ using fluorescence microscopy. The signal is bright for polarized mitochondria with high $\Delta\Psi_M$ and is dim when the mitochondrial membrane is depolarized. Despite being genetically identical and maintained under the same environment, we discovered different patterns of metabolic variability emerging at the multicellular level. Further, these variabilities showed different spatial patterns at different stages of CIP, as marked by the cell density (Fig. 1 *a*). In our study, we only considered epithelia post-confluence (i.e., packing fraction is one). Subsequently, at stage 1, which corresponded to the free-growing stage of CIP, cells showed cell-cell variability in $\Delta\Psi_M$ without any cluster formation (Fig. 1 *a*, *left*). At stage 2, which corresponded to the pre-epithelial transition stage of CIP, we noticed the emergence of cluster formation, with neighboring cells collectively having similar $\Delta\Psi_M$ (Fig. 1 *a*, *middle*; Fig. S1 *b*). Given the collective nature of the metabolic variability in this regimen, we termed this observation "collective heterogeneity." Finally, $\Delta\Psi_M$ appeared to be homogenized at stage 3, which corresponded to the post-epithelial transition stage of CIP (Fig. 1 *a*, *right*). The higher variability of $\Delta\Psi_M$ in stage 2 is confirmed by the higher variance compared with that of stages 2 and 3 (Fig. 1 *b*, *top*). To quantify the heterogeneity and spatial collectivity in $\Delta\Psi_M$, we defined a metric called heterogeneity index (ħ), which we defined as $\hbar = (\overline{I_{75\%}} - \overline{I_{25\%}}/\bar{I})$, where $\overline{I_{75\%}}$ and $\overline{I_{25\%}}$ are the mean fluorescence intensities of cells with top 25% and bottom 25% fluorescence intensity, respectively, and $\bar{I}$ represents the mean fluorescence intensity of the entire population. A perfectly homogeneous population will have $\hbar = 0$, and it should increase with increasing heterogeneity. Interestingly, at stage 2, cells show significantly higher ħ than cells at stages 1 and 3 (Fig. 1 *b*, *bottom*). Next, to extract spatial information, we first divided the image into ROIs of varying sizes. The mean ħ was then plotted against the ROI size to understand spatial information, as shown in Fig. S1 *c*. While ħ remained constant with decreasing ROI for cells at stages 1 and 3, for cells at stage 2, ħ decreased at the lowest size of ROI. This decrease in ħ occurred at the threshold length of ROI that matched the cluster size in the population because, when the ROI was less than or equal to the cluster of high- or low-potential cells, heterogeneity within the ROI decreased. As expected, stage 2 exhibited the highest relative change in ħ (Fig. S1 *d*), quantitatively representing the collective heterogeneity. Additionally, a significant fraction of the cell population showed vanishingly small $\Delta\Psi_M$ at stage 2 (Figs. 1 *c* and S1 *e*, red arrows). This population was unique to stage 2 and disappeared again at stage 3. The homogenous population at stage 3 implies that $\Delta\Psi_M$ of neighboring cells lost their correlation at this stage. This result is surprising given that the correlation length of cellular motions and forces monotonically increases with increasing density (15,36).

To check whether the metabolic variability was TMRM specific, in separate samples, we stained the cells with another $\Delta\Psi_M$ indicator dye, JC-1, where the measurement becomes ratiometric. JC-1 exhibits $\Delta\Psi_M$-dependent accumulation in mitochondria, indicated by a fluorescence emission shift from green (~525 nm) to red (~590 nm) as dye aggregates are formed from the monomers on the mitochondrial membranes. Hence, the red:green intensity ratio is high for polarized mitochondria and low for depolarized mitochondria. Moreover, the JC-1 signal is known to be independent of the morphological parameters of mitochondria. JC-1 staining also captured the different patterns of metabolic variability at different stages (Fig. S1 *f*). Like TMRM staining, we observed collective heterogeneity in JC-1 red emission at stage 2, and a more homogenous signal at stages 1 and 3 (Fig. S1 *f*). At stage 2, the distribution of JC-1 red:green intensity displayed two peaks, with one of the peaks located near zero (Fig. S1 *g*, red arrow). In contrast, at stages 1 and 3, we observed only a single peak in the distribution (Fig. S1 *g*). Hence, the results from JC-1 staining

experiments indicated that the observed density-dependent heterogeneity of the $\Delta\Psi_M$ was independent of the choice of dye. It is known that the cell division is not synchronized in a growing epithelial monolayer. Hence, to check whether the differences in cell cycle stages could be responsible for the observed heterogeneity in $\Delta\Psi_M$, we synchronized the cell cycle using the DNA polymerase alpha inhibitor aphidicolin and imaged the TMRM intensity landscape. The cell-cycle-synchronized population also exhibited collective heterogeneity in $\Delta\Psi_M$ at stage 2, thus undermining the contribution of cell cycle phases in metabolic heterogeneity (Fig. S2 *a*).

Further, we examined whether the heterogeneity arose from differential nutrition availability and cellular consumption. To this end, we first performed nutrient starvation experiments. We cultured MDCK cells at stage 2 in various minimal media instead of complete DMEM (see Materials and methods) and subsequently investigated the impact on collective heterogeneity in $\Delta\Psi_M$. We observed that the cells exhibited collective heterogeneity in $\Delta\Psi_M$ under all nutrient starvation conditions considered (Fig. S2 *b*), showing that nutrient availability did not play a major role in the emergence of collective heterogeneity in $\Delta\Psi_M$. To further understand the differences in nutrition availability, we measured the pyruvate, glucose, and lactate levels in cells by genetically encoded FRET-based sensors Pyronic, Laconic, and FLII12Pglu-700uDelta6, respectively. We transiently transfected MDCK cells with the corresponding plasmids and carried out FRET measurements in cells with high and low TMRM intensity. We did not observe any significant difference in the levels of glucose, lactate, or pyruvate in the two cell populations (Fig. S2 *c*), indicating that the corresponding nutrient availability in the cells is homogenous. Together, these two results demonstrated that the collective heterogeneity in Ψ_M did not originate from differential nutrient consumption or availability. Finally, we investigated whether differences in $\Delta\Psi_M$ stem from cell-cell differences in the mitochondrial mass. For this, we first stained cells at stage 2 with TMRM and imaged them. TMRM intensity appeared to be heterogeneous here. Later, we fixed the same sample and stained it with an antibody against a mitochondrial outer membrane protein, Tom20, that is commonly used to quantify the mitochondrial mass (37,38). Tom20 staining intensity appeared to be homogenous compared with the TMRM intensity landscape (Fig. 1 *d*). To evaluate how the mitochondrial content is different in the high and low $\Delta\Psi_M$ populations, we quantified the total Tom20 intensity in both populations. To this end, we considered the cells of lower-quartile TMRM intensity (the subpopulation of cells with the bottom-most 25% intensity) and upper-quartile TMRM intensity (the subpopulation of cells with the topmost 25% intensity) as the cells with low and high $\Delta\Psi_M$, respectively. A cell-wise quantification of the Tom20 signal showed that the population with higher $\Delta\Psi_M$ has a slightly higher Tom20 intensity compared with the population with lower $\Delta\Psi_M$. But the difference is low compared with the heterogeneity in $\Delta\Psi_M$. The enhancement in $\Delta\Psi_m$ ($\sim$3.59-fold) was significantly higher than that of the mitochondrial mass ($\sim$1.15-fold) (Fig. S2 *d*). Hence, we propose that the collective heterogeneity in $\Delta\Psi_M$ is not primarily due to the heterogeneity in the mitochondrial mass, although the latter may have some fractional contributions. Taken together, these results revealed a heterogeneous $\Delta\Psi_M$ field emerging in the epithelial monolayer whose length scale and variance depended on the global cell density. This heterogeneity was qualitatively and quantitatively different in three previously reported stages of CIP. Importantly, these results revealed an emergence of collective heterogeneity at stage 2, which is also the pre-epithelial transition stage. Hence, going forward, we investigated how this collective heterogeneity observed at stage 2 depended on the local parameters beyond its dependency on the global density.

Correlation of local variations in membrane potential with the local geometric environment

Relevantly, at stage 2, cells display a local fluctuation in density across the monolayer field (39,40). Hence, we next studied how the local fluctuation in density influences the metabolism in the pre-epithelial transition stage. For this purpose, we mapped the collective heterogeneity in metabolism, as measured by the spatial variation in TMRM intensity, onto the local number density of cells. To this end, we segmented the cell boundary from bright-field images using a custom-written code in MATLAB. The local density value was defined, by counting the number of cells around each pixel in a unit neighborhood area. The unit neighborhood area was defined as a square with a side of three times the average cell diameter because a side size of three times the average cell diameter was the optimum neighborhood area to give the maximum difference between average $\Delta\Psi_M$ for the low and high local density population of cells. (Fig. S3 *a*). Further correlation analysis showed that $\Delta\Psi_M$ was correlated with local variation of the number density of cells (Figs. 2 *a* and S3 *b*). To evaluate the statistical significance of this observed correlation, we compared the TMRM intensity of the top 25% dense region (high density) with that of the bottom 25% dense region (low density). The comparison revealed that TMRM intensity in high-density regions was higher than TMRM intensity in low-density regions (Fig. 2 *b*). Relevantly, local fluctuations in local density can result in changes in other geometric parameters of cells as well. We therefore investigated how different geometric parameters, including the cell area, cellular aspect ratio, and shape index are spatially correlated with TMRM intensity. Aspect ratio is defined as the ratio of the minor axis and major axis of the cell. The shape index is defined as the ratio of the perimeter to the square root of the area. We considered the cells of lower-quartile TMRM intensity

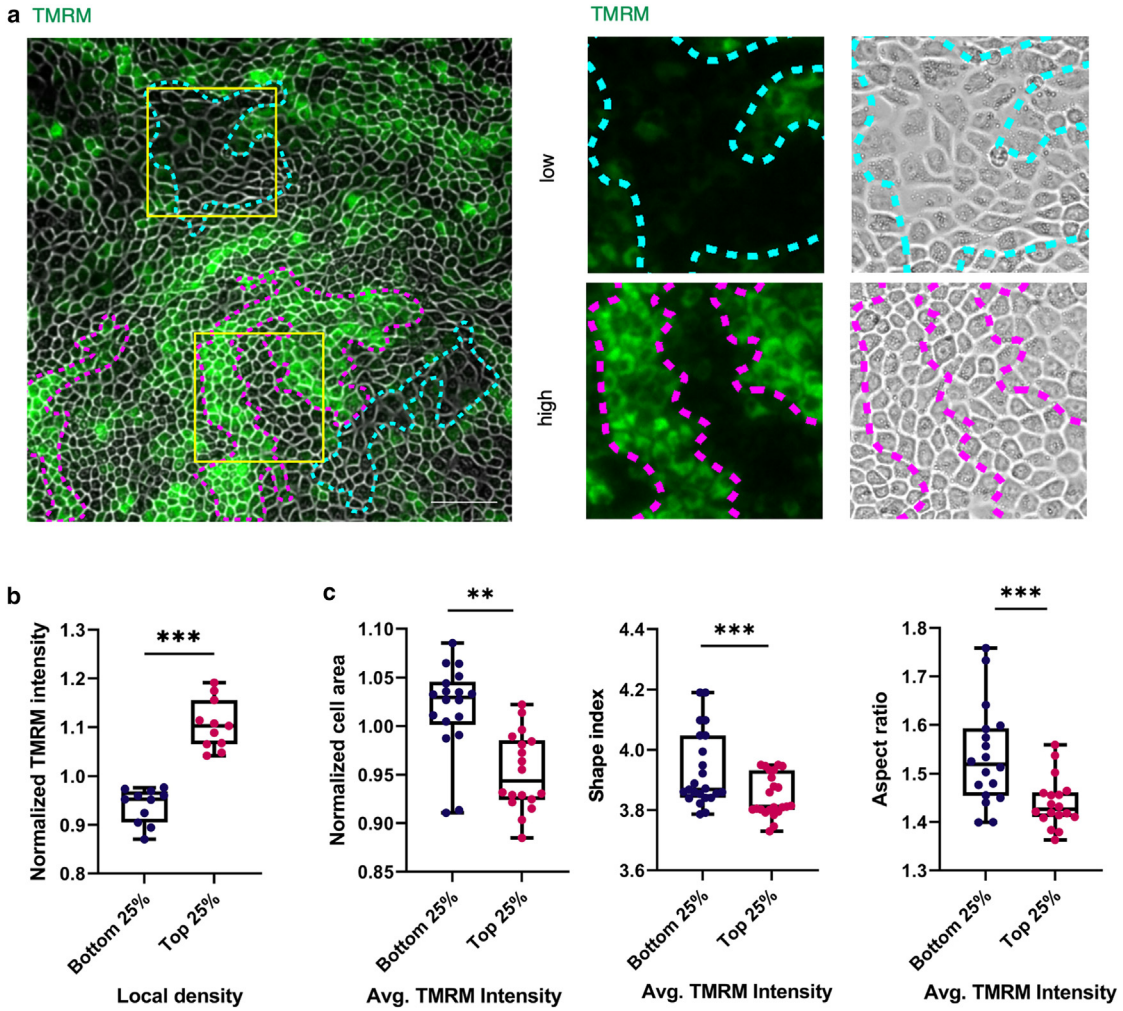

FIGURE 2 Local variations in membrane potential are correlated with the local geometric environment. (*a*) *Left panel*: Images of TMRM-stained MDCK cells, merged with bright-field images, showing cell boundaries. The increase and decrease in TMRM intensity correlate with the changes in local density. Magenta dashed lines mark high-$\Delta\Psi_M$ and cyan dashed lines mark low-$\Delta\Psi_M$ cells. Scale bar, 100 μm. *Right panel*: insets showing the high and low density corresponding to the changes in TMRM intensity. The yellow square in the *left panel* shows the cells used for insets. (*b*) Box-and-whisker plot showing the difference in mean TMRM intensity for MDCK cells at the highest (top 25%) and lowest (bottom 25%) local density neighborhood. Statistical significance was assessed using Wilcoxon matched-pairs signed-rank test. (*c*) *Left panel*: box-and-whisker plot showing the difference in mean area for MDCK cells with the highest (upper quartile) and lowest (lower quartile) TMRM intensity *Middle panel*: box-and-whisker plot showing the difference in mean shape index for MDCK cells with the highest (upper quartile) and lowest (lower quartile) TMRM intensity. *Right panel*: box-and-whisker plot showing the difference in mean aspect ratio for MDCK cells with the highest (upper quartile) and lowest (lower quartile) TMRM intensity. Statistical significance was assessed using Wilcoxon matched-pairs signed-rank test. *$p < 0.05$, **$p < 0.01$, and ***$p < 0.001$. To see this figure in color, go online.

and upper-quartile TMRM intensity as cells with low and high $\Delta\Psi_M$ for quantification purposes. The results delineating the variation of TMRM intensity with cell area revealed that the cells with high $\Delta\Psi_M$ were smaller compared with the cells with lower $\Delta\Psi_M$ (Fig. 2 *c left*). At the same time, the results delineating the variation of TMRM intensity with cellular aspect ratio and shape index revealed that the cells with high $\Delta\Psi_M$ were more rounded compared with cells with low $\Delta\Psi_M$, which were extended. (Fig. 2 *c*, *middle* and *right*). Interestingly, in all three stages, we observed that cells with higher TMRM intensity were smaller according to the normalized cell area (Fig. S3 *c*). Also, for cells at stage 3, there was no significant difference in aspect ratio and shape index for high and low TMRM intensity populations (Fig. S3 *c*). It is possible that, at this stage, cells are so crowded that they do not have enough flexibility to assume a variety of states in the physical space as well as in the biochemical space, as suggested by the relatively homogeneous mitochondrial potential field at this stage.

Further, to check how Tom20 level varies with cell shape or geometric features, we quantified the area, aspect ratio, and shape index of the cell population with the highest 25% Tom20 intensity and lowest 25% Tom20 intensity. Although Tom20 levels slightly increase with the increase in TMRM level, the geometric parameters do not follow

the same trend (Figs. 2 *c* and S3 *d*). Specifically, cells with high Tom20 intensity exhibit a larger area and higher shape index compared with the population with low Tom20 intensity. On the other hand, cells with high TMRM intensity display a smaller area and lower shape index compared with cells with low TMRM intensity (Figs. 2 *c* and S3 *d*). Again, in terms of the aspect ratio, cells with high and low Tom20 intensity follow the same trend as for TMRM intensity. Cells with high Tom20 intensity have a lower aspect ratio compared with the population with high Tom20 intensity and, hence, are more symmetrical. Cells with high TMRM intensity also have a lower aspect ratio (Figs. 2 *c* and S3 *d*, *right*). Together, these contrasts in the trends indicate that the correlation of heterogeneity in $\Delta\Psi_M$ with geometrical parameters cannot be attributed to the associated changes in mitochondrial mass. It is possible that cells of small areas in high-density regions may cause mitochondria to be tightly packed, resulting in a higher value of $\Delta\Psi_M$ when stained. However, we argue that it was not the case for these results because 1) there was high contrast in $\Delta\Psi_M$ between the population (Fig. S1 *b*) and 2) the heterogeneity of Tom20 signals was minuscule, which should not be the case if mitochondrial crowding because of cell size variation had a major effect on imaging. Taken together, these results show that, beyond global density, locally the heterogeneity in $\Delta\Psi_M$ is connected to the heterogeneity in geometric factors but not to biochemical factors, such as mitochondrial biogenesis.

Dynamic model

We next asked how metabolic heterogeneity is established as a function of cell proliferation. To this end, we constructed a phenomenological population-level dynamic model. Based on the results of the dependence of metabolic heterogeneity on density and CIP, we made two assumptions in the model: 1) cell proliferation decreases (therefore, proliferation time increases) sigmoidally with local cell density, and 2) $\Delta\Psi_M$, which is termed the "activation level" in the model, increases sigmoidally with local cell density. The sigmoidal dependence was chosen because of two reasons: 1) the proliferation capacity and activation threshold have an upper and lower bound, and 2) it allows quantifying two key parameters: threshold local densities that mark a steep transition from high to low proliferative capacity (division threshold) and that from a low to high $\Delta\Psi_M$ (activation threshold). These thresholds can potentially be determined experimentally using temporally collected images of cell culture. One crucial difference between the model and experimental condition is that the model does not operate at confluent conditions, but confluence is the final state of the model. This difference can be justified by the fact that the key assumptions are not dependent on the confluence but on local cell density, which can be captured by the measure of density defined in the model as the number of cells in a five-cell square (see Materials and methods).

Our model was able to capture the three stages of CIP-linked metabolic heterogeneity observed experimentally: sporadic activation at low density (stage 1), patches of activation representing collective heterogeneity (stage 2), and homogeneous activation (stage 3), as shown in Fig. 3 *a*. Stage 1 was characterized by a narrow distribution of activation with low mean. Stage 2 was characterized by the activation distribution skewed to the left, with patches of activation in the field, as mentioned above. Stage 3 was characterized by a narrow distribution with high mean activation (Fig. S4 *a*). Given the three phases, we wanted to identify factors that control the dynamics of these phases, specifically the residence time in each of the phases. As a first step, we focused on qualitative predictions that can be verified experimentally. First, we tried to understand the appearance of collective heterogeneity as a function of the threshold of activation and threshold of proliferation. Given the distribution characteristics above, we tracked the dynamics of the variance of cell activation level distribution with time as a metric to distinguish between the three stages (Fig. 3 *b*; Video S1a).

At a high activation threshold, a low division threshold allows clear emergence and longer sustenance of stage 2, where collective heterogeneity exists (Fig. 3 *c*; Video S1a). At higher division thresholds, stage 2 emerges but remains for a relatively shorter period (Fig. 3 *c*; Video S1b). At a lower activation threshold, on the other hand, we found multiple short-lived patches of high variance activation profiles (Fig. 3 *d*; Video S1c) for each division time. These results can be interpreted as the fact that a lower activation threshold allows quick homogenization of the system, thereby reducing the chances of emergence of heterogeneity. This is also the reason why the system requires a high exponent for activation-level dependence on density (nAct) (Fig. 3 *e*), which is the exponent in the activation-level equation (Eq. 1). Because the division threshold has a relatively lesser impact on the system, collective heterogeneity is not sensitive to nDiv (Fig. S4 *b*), which is the exponent in the division time equation (Eq. 2).

Furthermore, we predicted that the dependence of activation and proliferation must be on local density (small R) as opposed to global density because the dependence of $\Delta\Psi_M$ on global density leads to rapid homogenization of $\Delta\Psi_M$, thereby eliminating the existence of collective heterogeneity. The neighborhood parameter R in our model determined whether a cell was sensitive to local density (low value of R) or global density (high value of R). We found that, as the value of R increased, the variance in activation level that distinguishes collective heterogeneity goes down, being comparable with the variance of low- and high-density scenarios at $R = 9$ (Fig. 3 *f*).

Our sensitivity analysis (all figures are included in the GitHub repository) hence shows that, among the seven

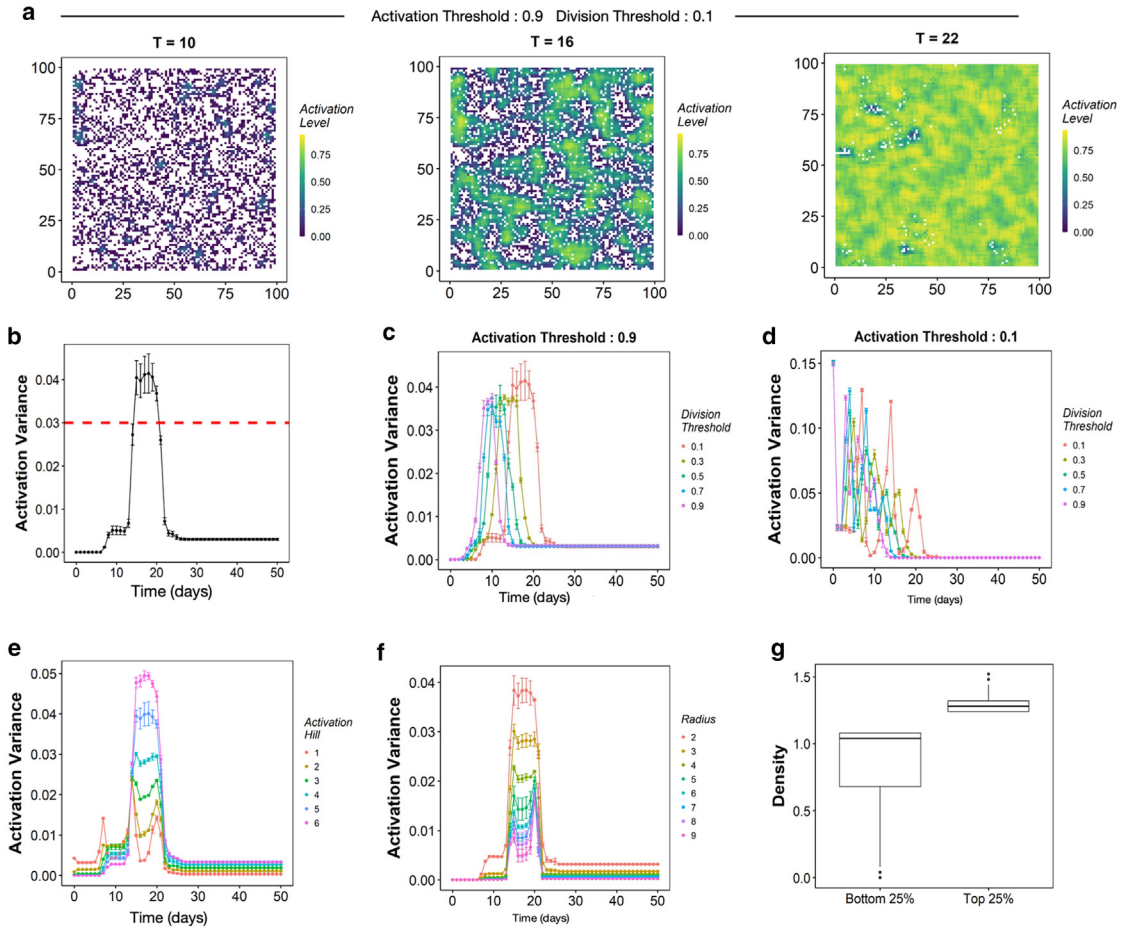

FIGURE 3 Results from the simulation. (*a*) Activation level heatmaps at different time points (T = 10, 16, 22) corresponding to 3 stages. Each pixel represents a cell in the figure. (*b*) Line plot showing activation variance against time points (each time point corresponds to different densities). (*c*) Line plot showing activation variance for different division threshold values with high actThresh (0.9). (*d*) Same as (*c*) but for a low actThresh (0.1). (*e*) Line plot showing activation variance against the Hill coefficient corresponding to activation level. (*f*) Line plot showing activation variance against the neighborhood radius. Maximum variance is obtained at a two- to three-cell neighborhood radius. (*g*) Boxplot depicting density differences in cells with low and high activation levels. **p $<$ 0.01. To see this figure in color, go online.

parameters considered in the model, the emergence of collective heterogeneity is mainly sensitive to three parameters: high activation threshold (actThresh; >0.5), high nAct (Eq. 1; >3), and low neighborhood parameter (R $<$ 4), which represents the sensitivity of each cell to its surroundings. Sensitivity analysis clearly shows that, while changing the other parameters (including division Hill [Fig. S4 *b*], division time [Fig. S4 *c*], and division time FC [Fig. S4 *d*]) might have minor quantitative changes in the collective heterogeneity dynamics, qualitatively they remain the same. The details of all parameters and the sensitivity analysis have been described in the Materials and methods section. The density around the cell also controls the relevant mechanical parameters; hence, we use the density parameter in the model as a proxy of the mechanical aspects, such as intracellular pressure. Cells with lower $\Delta\Psi_M$ delve into lower-density regions and therefore have lower intracellular pressure. Similarly, cells with higher $\Delta\Psi_M$ have a higher density and therefore higher pressure (Fig. 3 *g*). Taken together, the simulation results predicted a role of cell proliferation in metabolic potential toward setting the collective heterogeneity in the latter at the medium density corresponding to stage 2 of CIP.

Metabolism pattern emergence is correlated to the proliferation capacity of cells

Next, to test this prediction from the dynamic model, we studied $\Delta\Psi_M$ and the proliferation capacity of cells in the same sample. As a proxy for proliferation capacity, we used nuclear/cytoplasmic (N/C) localization of a transcriptional regulator protein, YAP (yes-associated protein 1). We preferred it over EdU staining because we reasoned that EdU-positive S phase cells would be time-wise advanced in the cell cycle. In that case, even if a change in the metabolic potential had initiated proliferation earlier, S phase cells might not be correlated with the spatial distribution of metabolic patterns at the time of observation. On

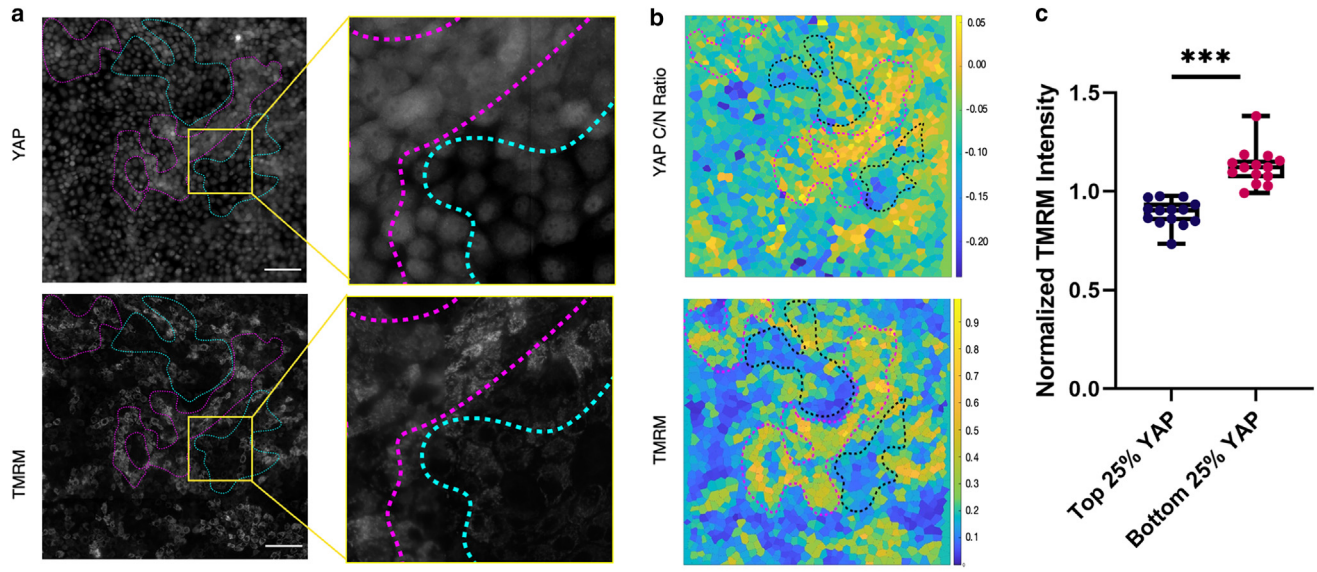

FIGURE 4 Metabolic heterogeneity is correlated with the proliferation capacity of the cells. (*a*) Fluorescence images comparing YAP N/C localization (*top panel*) and TMRM levels (*bottom panel*) in MDCK cells at stage 2 of CIP. Nuclear localization of YAP corresponding with low TMRM intensity is marked with cyan dashed lines. Cytoplasmic localization of YAP corresponding with high TMRM intensity is marked with magenta dashed lines. On the right, insets are shown at higher magnification. Scale bars, 100 μm. (*b*) Heatmaps showing mean TMRM levels (*bottom panel*) and YAP N/C (*top panel*) in MDCK cells. Dashed lines show the cell population with high and low TMRM intensity and YAP C/N ratio. (*c*) Box-and-whisker plot showing the difference in mean TMRM intensity in the cell population having the lowest (lower quartile) and highest (upper quartile) N/C ratio of YAP. Statistical significance was assessed using the Wilcoxon matched-pairs signed-rank test. ***$p < 0.001$. To see this figure in color, go online.

the other hand, YAP is a protein that, when localized to the nucleus, induces division by activating genes involved in proliferation and suppressing those involved in apoptosis. Nuclear localized YAP suggests a proliferative cell, and cytoplasmic localization suggests inhibited proliferation (18). YAP nuclear localization, therefore, indicates a very early stage of pro-proliferation activity, perhaps right at the moment when the change in metabolism triggers proliferation. First, to understand how the proliferation capacity of cells changes collectively at different stages of CIP, we immunostained confluent MDCK cells with a YAP antibody at different densities. At stage 1, all cells have nuclear localization of YAP. At stage 2, cells appear as patches in terms of YAP N/C localization, like the collective heterogeneity in metabolism. At stage 3, all cells have cytoplasmic localization of YAP (Fig. S5 *a*). The results indicate that the variability of proliferative capacity among cells is similar to that of $\Delta\Psi_M$, especially the appearance of collective patches in stage 2. Nevertheless, we also studied the pattern of EdU staining and observed emergence of clustering at stage 2 there as well (Fig. S5 *b*). In contrast, at stage 3, most cells were found to be EdU negative, and at stage 1, EdU-positive cells were found to be distributed evenly in the field of view. We next studied the local correlation of proliferation capacity with $\Delta\Psi_M$ at stage 2. To this end, we stained the cells at stage 2 with TMRM to measure $\Delta\Psi_M$. We then fixed and immunostained the same cells with YAP to find that YAP N/C localization was correlated with $\Delta\Psi_M$. Low-$\Delta\Psi_M$ regions were associated with cells having predominantly nuclear YAP localization, while high-$\Delta\Psi_M$ regions were associated with cells having predominantly cytoplasmic YAP localization (Fig. 4 *a* and *b*). For quantification, we considered cells of lower quartile TMRM intensity and upper quartile TMRM intensity as cells with low and high $\Delta\Psi_M$. The results delineating the variation of TMRM intensity with YAP nuclear translocation revealed that cells with low $\Delta\Psi_M$ have proliferation capacity, while cells with higher $\Delta\Psi_M$ are entering quiescence. Cells with low $\Delta\Psi_M$ have high nuclear translocation of YAP compared with the cells with high $\Delta\Psi_M$ (Fig. 4 *c*). Together, these results upheld the predicted correlation between proliferative capacity, as represented by the nuclear localization of YAP, and metabolic heterogeneity, suggesting a connection between these two aspects of a confluent epithelial monolayer.

Metabolic memory and dependence of collective heterogeneity on the active mechanical state

To summarize the results obtained so far, we showed that the collective heterogeneity in metabolism is associated with local density fluctuations and proliferation. Notably, local density fluctuations and proliferation are mechanosensitive events. With local density fluctuation of the epithelial monolayer, actomyosin content and organization, key players in cell mechanics, are known to change (41,42). The proliferation regulator YAP/TAZ is also mechanosensitive (42). In addition, CIP ceases to happen in the absence of

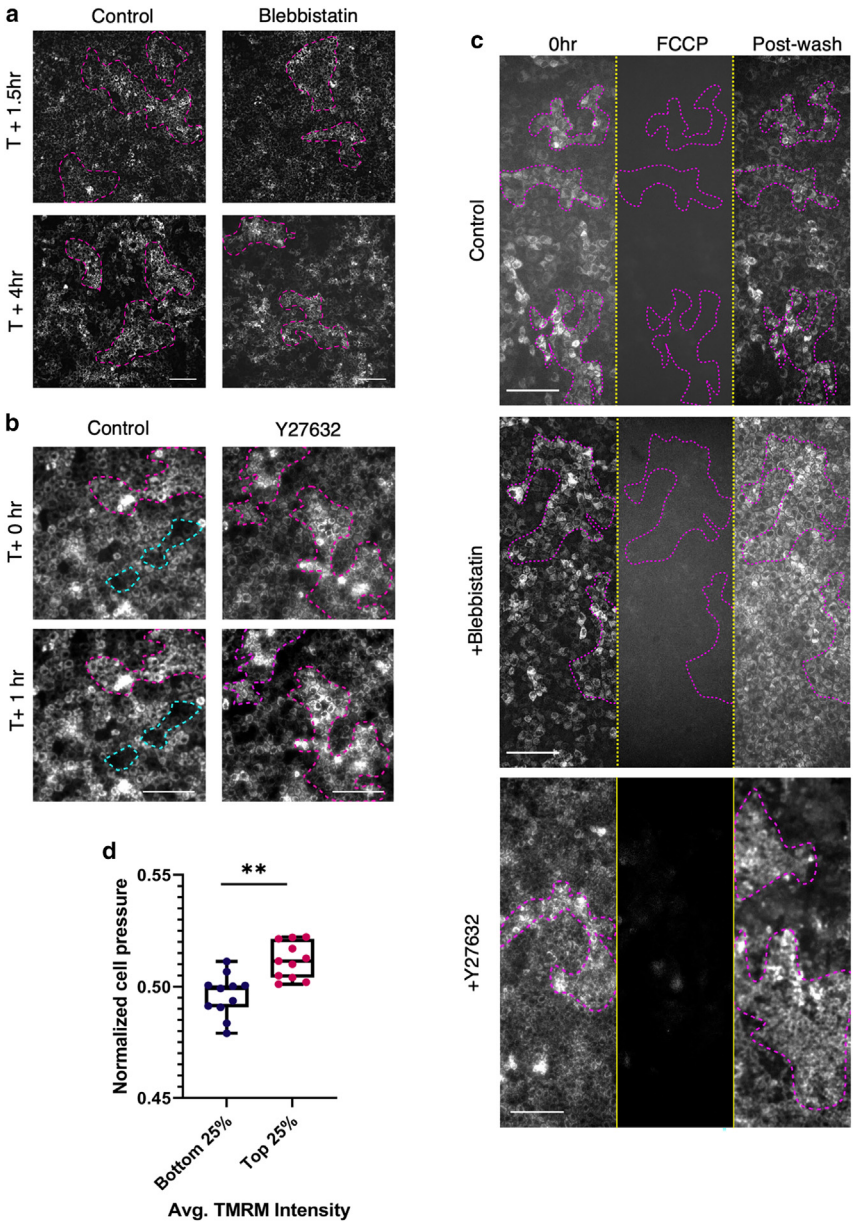

FIGURE 5 Metabolic memory and dependence of collective heterogeneity on active mechanical state. (*a*) Images of a TMRM-stained MDCK cell monolayer at stage 2, showing patterns of TMRM heterogeneity. Treatment with blebbistatin without FCCP does not get rid of metabolic heterogeneity. *Left panels*: control. *Right panels:* blebbistatin treated. Magenta dashed lines show high-TMRM-intensity clusters. Scale bar, 100 μm. (*b*) Images of a TMRM-stained MDCK cell monolayer at stage 2 of CIP. Treatment with Y27632 without FCCP does not get rid of metabolic heterogeneity. *Left panels*: control. *Right panels:* Y27632 treated. Magenta and cyan dashed lines show high- and low-TMRM-intensity clusters, respectively. Scale bar, 50 μm. (*c*) A time-lapse montage of a TMRM-stained MDCK monolayer at stage 2. Left to right: before FCCP treatment, after FCCP treatment, and after washing off FCCP with replacement of complete DMEM. *Top panel*: vehicle wash-off medium could bring back the initial metabolic heterogeneity patterns in the monolayer. *Middle panel*: wash-off medium with blebbistatin is used, and heterogeneity is lost in this case post washing. Scale bar, 100 μm. The collective heterogeneity pattern is highlighted with magenta dashed lines. *Bottom panel*: wash-off medium with Y27632 is used, and the pattern of heterogeneity is changed in this case post washing. The collective heterogeneity pattern is highlighted with magenta dashed lines. Scale bar, 100 μm. (*d*) Box-and-whisker plot showing the difference in mean TMRM intensity in a cell population having the lowest (bottom 25%) and highest (top 25%) cell pressure. Statistical significance was assessed using the Wilcoxon matched-pairs signed-rank test. $^{**}p < 0.01$. To see this figure in color, go online.

adhesion molecules or under actomyosin inhibition conditions (43,44). Last, mechanical stretch can increase proliferation, acting through the Hippo pathway (43). Hence, we next asked whether actomyosin contractility is necessary to maintain and/or establish metabolic collective heterogeneity. First, to check whether cells can maintain collective heterogeneity in the absence of actomyosin contractility, we treated the cell monolayer at stage 2 with a myosin inhibitor, blebbistatin, that is known to reduce actomyosin contractility. After the treatment, we tracked the cells for 4 h but did not observe any change in metabolic heterogeneity (Fig. 5 *a*). Similarly, treatment of the cells with Y27632, a ROCK inhibitor did not cause any change in metabolic heterogeneity over time (Fig. 5 *b*). This experiment indicated that maintenance of collective heterogeneity does not depend on active cellular mechanics. Second, to check whether the establishment of collective heterogeneity requires actomyosin contractility, we first abolished the $\Delta\Psi_M$ in all cells by treating the cells with an H^+ ionophore and uncoupler of oxidative phosphorylation, FCCP, and then studied how the cells regained $\Delta\Psi_M$ upon withdrawal of FCCP from the medium in the presence and absence of blebbistatin and Y27632. As expected, FCCP treatment homogenously depolarized the mitochondria of all cells in the monolayer (Fig. 5 *c*). When FCCP was washed off post treatment and normal DMEM was added, the cells re-established the same pattern of collective heterogeneity they had before depolarization (Fig. 5 *c*, *top*). However, when the recovery DMEM contained blebbistatin, the cells regained their $\Delta\Psi_M$, but the collective heterogeneity of $\Delta\Psi_M$

vanished and a metabolically homogenous population emerged (Fig. 5 *c*, *middle*). When the recovery DMEM contained Y27632, the cells regained their $\Delta\Psi_M$, but with a visibly different pattern of collective heterogeneity of $\Delta\Psi_M$. In contrast to blebbistatin treatment, ROCK inhibition did not homogenize the $\Delta\Psi_M$ (Fig. 5 *c*, *bottom*). These results revealed that, when emerged, epithelial cells can maintain metabolic heterogeneity in the absence of actomyosin contractility. However, its initial emergence depended on the latter. These results are quantified in Fig. S6, *a–d*. Only when the cells are treated with blebbistatin, post FCCP treatment, ħ decreases and stays constant independent of the ROI size, indicating emergence of a homogenous population (Fig. S6 *d*). In all other cases, we observe a drop in ħ with a decrease in ROI size, signifying collective heterogeneity (Fig. S6 *a–d*). To better understand the different effects of FCCP wash-off followed by blebbistatin or Y27632, we went on to analyze the accompanied changes in cellular geometry. To this end, we analyzed the shape index and aspect ratio before and after treatment in both cases (Fig. S6 *e–h*). We did not see any noticeable global shift in cell shape in either case (Fig. S6 *e* and *h*). Although FCCP treatment followed by blebbistatin homogenized the $\Delta\Psi_M$, it did not lead to a homogenous cell population in terms of the cell shape parameters (Fig. S6 *e*). On the other hand, local changes in cell shape were observed in case of FCCP + Y27632 treatment. These changes in cell shape were predominantly localized to regions where the heterogeneity pattern of the cells changed (Fig. S6 *f* and *g*). This suggests that the effect of blebbistatin can be attributed to its negative impact on the mechanosensing ability of cells. In contrast, Y27632 alters the geometric parameters to change the mitochondrial potential heterogeneity landscape.

Finally, we investigated whether there exists a direct correlation between the local mechanical state and collective metabolic heterogeneity. To this end, we calculated the cell-cell junctional tension and pressure using the Bayesian force inference method (33) and, at the same time, stained the cells with TMRM (Fig. S6 *i*). For quantification, we considered cells of lower-quartile TMRM intensity and upper-quartile TMRM intensity as cells with low and high $\Delta\Psi_M$. The results delineating the variation of TMRM intensity with cell pressure revealed that cells with high $\Delta\Psi_M$ have higher intracellular pressure compared with cells with lower $\Delta\Psi_M$ (Fig. 5 *d*). Together, these results indicate the importance of active cellular mechanics for establishment of collective heterogeneity in metabolism. However, maintenance of metabolic variability does not depend on actomyosin contractility, only *ab initio* emergence does.

DISCUSSION

Taken together, our experiments unveiled the heterogeneous landscape of metabolism in epithelial cells. The length scale of this heterogeneity changes as the cells transition through three stages of CIP. Significantly, we unveil collective heterogeneity in $\Delta\Psi_M$ at stage 2 of CIP (Fig. 1). The system under our study is a monolayer of genetically identical epithelial cell populations, all under the same nutrient conditions. Hence, the self-emergence of a collective-level heterogeneity in $\Delta\Psi_M$ in the absence of any external signaling in an otherwise identical environment is of great interest. Through experimental characterization and the systems biology model, we suggest that epithelial cells bring about these biochemical variabilities because of their intricate relations with emerging biophysical differences. Relevantly, the biophysical differences in terms of geometrical and certain cell mechanics-related parameters of the cells are basically a result of the non-uniform growth in the monolayer. Non-uniform growth gives rise to feedback mechanical signals to ensure uniform growth (40). Hence, we speculate that the metabolic variabilities in cells lead to mechanical variabilities. However, further studies are required for a deeper understanding.

The mathematical model implemented in this manuscript has been designed to be a minimalistic one. Parameters related to cell mechanics or cell geometry, for instance, have not been explicitly included in the model. While the importance of these parameters cannot be ignored, because the aim of the investigation is to determine the effect of density on cell proliferation and metabolic activity, we introduced phenomenological parameters, such as the density threshold and radius of sensitivity, to explain how collective heterogeneity may arise in metabolic activity. As we have briefly shown, the cell mechanics parameters correlate well with density, and, hence, the effect of these parameters on collective heterogeneity can be predicted based on the current modeling formalism. In the future, we plan to expand the scope of the model by explicitly including the mechanical and geometric parameters and investigate their impact on collective heterogeneity as well.

We found that $\Delta\Psi_M$ variabilities were correlated with the proliferative capacity of cells (Fig. 4). Quiescent cells have higher $\Delta\Psi_M$, while proliferating cells have less. It is possible that this is because proliferating cells prefer the glycolytic pathway rather than oxidative phosphorylation for their energy requirements, hence staying at the basal $\Delta\Psi_M$ level, an effect similar to the Warburg effect (22). Interestingly, similar density-dependent changes have been observed in contact inhibition of locomotion (CIL), in the case of jamming transition in epithelial cells (15,45). In jamming-transition, as density increases, the velocity of cells decreases but the fastest cells move in large multicellular groups (15). Cells become less elongated and less variable, as they get approach jamming (46). It also is known that during epithelial unjamming, energy metabolism shifts toward the glycolysis (47), which connects CIL to local changes in metabolism. In our work, we reveal the local changes in metabolism with CIP. Hence, these results together indicate that density-dependent changes in cellular metabolism are fundamental properties of

the epithelial tissue in the context of CIP and CIL, which should have enormous physiological consequences.

In this regard, one of the main physiological implications of density-dependent collective heterogeneity will be pattern formation in multicellular organisms. Hair follicle distribution in mammalian skin is a scenario where this may be relevant. Which cells among the skin give rise to placodes and the determining factor are still not completely understood (48,49). Given the density and shape changes in cells during placode formation, it will be interesting to look at metabolic and biophysical changes before initiation of placode formation. Because we used a monolayer of epithelial cells for the current study, fundamental characteristics of the epithelium in the absence of any external signaling can be pinpointed here. At the same time, this becomes a limitation because it is not the case under physiological conditions. Investigation of the local metabolic changes in a 3D organoid model along with the biophysical characterization will be an interesting study. We also concentrated solely on $\Delta\Psi_M$ reading as a proxy for metabolism. Complete metabolic profiling as the cells progress through CIP with increasing density will be a worthwhile endeavor, given the results from our current study.

CONCLUSIONS

While the metabolic changes in a cell population as CIP sets in have been investigated, the patterns of local metabolic changes as the cells progress through CIP are relatively less known. We systematically studied the local changes in metabolism during CIP, using $\Delta\Psi_M$ measurement as a proxy for metabolism. Collectively, our experiments established three different metabolic regimens corresponding to the three different stages of CIP (Fig. 1 *a*). At stage 1, cells showed cell-cell variability in $\Delta\Psi_M$ without any cluster formation. We unveil emergence of multicellular-level collective heterogeneity in $\Delta\Psi_M$ at stage 2 of CIP. Importantly, this collective heterogeneity in $\Delta\Psi_M$ was exclusive to stage 2 and disappeared at stage 3, while other parameters such as the correlation length of cellular motions and the monolayer stresses monotonically increase with increasing density. Our further investigations show that the metabolic changes are correlated with the local changes in cell density and the geometric parameters of cells (Fig. 2). We found that, at stage 2, cells with comparatively higher $\Delta\Psi_M$ are smaller, rounder, and more symmetric compared with the cells with lower $\Delta\Psi_M$. While the connection between CIP and mechanics has been shown previously (4,50), here we demonstrate that the local metabolic changes that accompany CIP are also connected to cell mechanics (Fig. 5). A simple mathematical model could capture the three different metabolic regimens corresponding to the three stages of CIP. The model where the cellular parameters depend on local density predicted a role of cell proliferation in collective heterogeneity at stage 2 of CIP. Subsequently, *in vitro*, we found that the $\Delta\Psi_M$ variabilities were correlated with the proliferation capacity of cells (Fig. 4). Altogether, we reveal a heterogeneous landscape of $\Delta\Psi_M$ emerging in the epithelial monolayer, whose length scale depends on the global density of cells. The heterogeneous landscape observed is different in the three stages of CIP. Importantly, for the first time, we reveal emergence of collective heterogeneity in the otherwise identical epithelial cells at stage 2 of CIP, which is related to the geometric and mechanical parameters of the cell.

DATA AND CODE AVAILABILITY

The simulation and analysis codes of the model and the experimental images are provided in the GitHub repository https://github.com/askhari139/CollectiveHeterogeeneity. The figures corresponding to the sensitivity analysis of all model parameters are available in the repository as well.

SUPPORTING MATERIAL

Supporting material can be found online at https://doi.org/10.1016/j.bpj.2023.08.014.

AUTHOR CONTRIBUTIONS

B.T., R.M., and S.K. performed the experiments. K.H. performed the model simulation. B.T., S.K., and T.D. conceived the project. T.D. supervised the experimental part, while M.K.J. supervised the modeling part. B.T., K.H., M.K.J., and T.D. wrote the manuscript. All authors commented on the manuscript.

ACKNOWLEDGMENTS

We thank the Collective Cellular Dynamics (CCD) laboratory members for critical discussions, Raphaël Clément for the source code of the Bayesian force inference program, and Manish Jaiswal and (the late) Surajit Sengupta for comments and suggestions. T.D. is a DBT/Wellcome Trust India Alliance intermediate fellow and partner group leader of the Max Planck Society (MPG), Germany. This work is funded by DBT/Wellcome Trust India Alliance (grant IA/I/17/1/503095 to T.D.). We also acknowledge intramural funds from the Tata Institute of Fundamental Research, Hyderabad, and the Department of Atomic Energy Energy, India (under project ID RTI 4007) and generous funding from the Human Frontier Science Program (HFSP; grant RGP0007/2022).

DECLARATION OF INTERESTS

The authors declare no competing interests.

REFERENCES

1. Lecuit, T., and L. Le Goff. 2007. Orchestrating size and shape during morphogenesis. *Nature*. 450:189–192.
2. Castor, L. N. 1968. Contact regulation of cell division in an epithelial-like cell line. *J. Cell. Physiol.* 72:161–172.
3. Stoker, M. G., and H. Rubin. 1967. Density dependent inhibition of cell growth in culture. *Nature*. 215:171–172.

4. Puliafito, A., L. Hufnagel, …, B. I. Shraiman. 2012. Collective and single cell behavior in epithelial contact inhibition. *Proc. Natl. Acad. Sci. USA.* 109:739–744.
5. Hanahan, D., and R. A. Weinberg. 2000. The hallmarks of cancer. *Cell.* 100:57–70.
6. Aragona, M., T. Panciera, …, S. Piccolo. 2013. A mechanical checkpoint controls multicellular growth through YAP/TAZ regulation by actin-processing factors. *Cell.* 154:1047–1059.
7. Steinberg, M. S., and P. M. McNutt. 1999. Cadherins and their connections: adhesion junctions have broader functions. *Curr. Opin. Cell Biol.* 11:554–560.
8. Weis, W. I., and W. J. Nelson. 2006. Re-solving the cadherin-catenin-actin conundrum. *J. Biol. Chem.* 281:35593–35597.
9. Nelson, C. M., R. P. Jean, …, C. S. Chen. 2005. Emergent patterns of growth controlled by multicellular form and mechanics. *Proc. Natl. Acad. Sci. USA.* 102:11594–11599.
10. Kim, J. H., K. Kushiro, …, A. R. Asthagiri. 2009. Tunable interplay between epidermal growth factor and cell-cell contact governs the spatial dynamics of epithelial growth. *Proc. Natl. Acad. Sci. USA.* 106:11149–11153.
11. Kim, N. G., E. Koh, …, B. M. Gumbiner. 2011. E-cadherin mediates contact inhibition of proliferation through Hippo signaling-pathway components. *Proc. Natl. Acad. Sci. USA.* 108:11930–11935.
12. McClatchey, A. I., and A. S. Yap. 2012. Contact inhibition (of proliferation) redux. *Curr. Opin. Cell Biol.* 24:685–694.
13. Streichan, S. J., C. R. Hoerner, …, L. Hufnagel. 2014. Spatial constraints control cell proliferation in tissues. *Proc. Natl. Acad. Sci. USA.* 111:5586–5591.
14. Zhao, B., X. Wei, …, K. L. Guan. 2007. Inactivation of YAP oncoprotein by the Hippo pathway is involved in cell contact inhibition and tissue growth control. *Genes Dev.* 21:2747–2761.
15. Angelini, T. E., E. Hannezo, …, D. A. Weitz. 2011. Glass-like dynamics of collective cell migration. *Proc. Natl. Acad. Sci. USA.* 108:4714–4719.
16. Zhao, B., X. Ye, …, K. L. Guan. 2008. TEAD mediates YAP-dependent gene induction and growth control. *Genes Dev.* 22:1962–1971.
17. Schlegelmilch, K., M. Mohseni, …, F. D. Camargo. 2011. Yap1 acts downstream of alpha-catenin to control epidermal proliferation. *Cell.* 144:782–795.
18. Varelas, X. 2014. The Hippo pathway effectors TAZ and YAP in development, homeostasis and disease. *Development.* 141:1614–1626.
19. Locasale, J. W., and L. C. Cantley. 2011. Metabolic flux and the regulation of mammalian cell growth. *Cell Metabol.* 14:443–451.
20. Warburg, O. 1956. On the origin of cancer cells. *Science.* 123:309–314.
21. Martins, S. F., R. Amorim, …, F. Baltazar. 2016. Significance of glycolytic metabolism-related protein expression in colorectal cancer, lymph node and hepatic metastasis. *BMC Cancer.* 16:535.
22. Vander Heiden, M. G., L. C. Cantley, and C. B. Thompson. 2009. Understanding the Warburg effect: the metabolic requirements of cell proliferation. *Science.* 324:1029–1033.
23. Spinelli, J. B., and M. C. Haigis. 2018. The multifaceted contributions of mitochondria to cellular metabolism. *Nat. Cell Biol.* 20:745–754.
24. Zamzami, N., P. Marchetti, …, G. Kroemer. 1995. Sequential reduction of mitochondrial transmembrane potential and generation of reactive oxygen species in early programmed cell death. *J. Exp. Med.* 182:367–377.
25. Zamzami, N., S. A. Susin, …, G. Kroemer. 1996. Mitochondrial control of nuclear apoptosis. *J. Exp. Med.* 183:1533–1544.
26. Liu, X., C. N. Kim, …, X. Wang. 1996. Induction of apoptotic program in cell-free extracts: requirement for dATP and cytochrome c. *Cell.* 86:147–157.
27. Bereiter-Hahn, J., A. Münnich, and P. Woiteneck. 1998. Dependence of energy metabolism on the density of cells in culture. *Cell Struct. Funct.* 23:85–93.
28. Cho, M. J., D. P. Thompson, …, J. F. Scieszka. 1989. The Madin Darby canine kidney (MDCK) epithelial cell monolayer as a model cellular transport barrier. *Pharm. Res. (N. Y.).* 6:71–77.
29. Datseris, G., A. R. Vahdati, and T. C. DuBois. 2022. Agents.jl: a performant and feature-full agent-based modeling software of minimal code complexity. *Simulation.* 0, 003754972110688.
30. Aigouy, B., and B. Prud'homme. 2022. Prud'homme. *Methods Mol. Biol.* 2540:387–399.
31. Stringer, C., T. Wang, …, M. Pachitariu. 2021. Cellpose: a generalist algorithm for cellular segmentation. *Nat. Methods.* 18:100–106.
32. Sero, J. E., and C. Bakal. 2017. Multiparametric Analysis of Cell Shape Demonstrates that beta-PIX Directly Couples YAP Activation to Extracellular Matrix Adhesion. *Cell Syst.* 4:84–96.e6.
33. Ishihara, S., and K. Sugimura. 2012. Bayesian inference of force dynamics during morphogenesis. *J. Theor. Biol.* 313:201–211.
34. Kong, W., O. Loison, …, R. Clément. 2019. Experimental validation of force inference in epithelia from cell to tissue scale. *Sci. Rep.* 9, 14647.
35. Scaduto, R. C., Jr., and L. W. Grotyohann. 1999. Measurement of mitochondrial membrane potential using fluorescent rhodamine derivatives. *Biophys. J.* 76:469–477.
36. Vishwakarma, M., B. Thurakkal, …, T. Das. 2020. Dynamic heterogeneity influences the leader-follower dynamics during epithelial wound closure. *Philos. Trans. R. Soc. Lond. B Biol. Sci.* 375, 20190391.
37. Burbulla, L. F., J. C. Fitzgerald, …, R. Krüger. 2014. Mitochondrial proteolytic stress induced by loss of mortalin function is rescued by Parkin and PINK1. *Cell Death Dis.* 5:e1180.
38. Begum, H. M., H. P. Ta, …, K. Shen. 2019. Spatial Regulation of Mitochondrial Heterogeneity by Stromal Confinement in Micropatterned Tumor Models. *Sci. Rep.* 9, 11187.
39. Zehnder, S. M., M. K. Wiatt, …, T. E. Angelini. 2015. Multicellular density fluctuations in epithelial monolayers. *Phys. Rev. E - Stat. Nonlinear Soft Matter Phys.* 92, 032729.
40. Shraiman, B. I. 2005. Mechanical feedback as a possible regulator of tissue growth. *Proc. Natl. Acad. Sci. USA.* 102:3318–3323.
41. Loza, A. J., S. Koride, …, G. D. Longmore. 2016. Cell density and actomyosin contractility control the organization of migrating collectives within an epithelium. *Mol. Biol. Cell.* 27:3459–3470.
42. Peyret, G., R. Mueller, …, B. Ladoux. 2019. Sustained Oscillations of Epithelial Cell Sheets. *Biophys. J.* 117:464–478.
43. Hirata, H., M. Samsonov, and M. Sokabe. 2017. Actomyosin contractility provokes contact inhibition in E-cadherin-ligated keratinocytes. *Sci. Rep.* 7, 46326.
44. St Croix, B., C. Sheehan, …, R. S. Kerbel. 1998. E-Cadherin-dependent growth suppression is mediated by the cyclin-dependent kinase inhibitor p27(KIP1). *J. Cell Biol.* 142:557–571.
45. Stramer, B., and R. Mayor. 2017. Mechanisms and in vivo functions of contact inhibition of locomotion. *Nat. Rev. Mol. Cell Biol.* 18:43–55.
46. Atia, L., D. Bi, …, J. J. Fredberg. 2018. Geometric constraints during epithelial jamming. *Nat. Phys.* 14:613–620.
47. DeCamp, S. J., V. M. K. Tsuda, …, J. J. Fredberg. 2020. Epithelial layer unjamming shifts energy metabolism toward glycolysis. *Sci. Rep.* 10, 18302.
48. Stark, J., T. Andl, and S. E. Millar. 2007. Hairy math: insights into hair-follicle spacing and orientation. *Cell.* 128:17–20.
49. Harn, H. I. C., S. P. Wang, …, C. M. Chuong. 2021. Symmetry breaking of tissue mechanics in wound induced hair follicle regeneration of laboratory and spiny mice. *Nat. Commun.* 12:2595.
50. Irvine, K. D., and B. I. Shraiman. 2017. Mechanical control of growth: ideas, facts and challenges. *Development.* 144:4238–4248.